Biomaterials Science

ROYAL SOCIETY OF CHEMISTRY

PAPER

View Article Online
View Journal | View Issue

Cite this: *Biomater. Sci.*, 2025, **13**, 1784

Hollow nanosystem-boosting synergistic effects between photothermal therapy and chemodynamic therapy *via* self-supplied hydrogen peroxide and relieved hypoxia†

Yunji Sun, [a,b] Lixiao Zhen,[a] Lin Xu,[a] Peipei Li,[a] Chao Zhang,[b] Yang Zhang,*[d] Yisheng Zhao*[c] and Benkang Shi*[b]

Received 6th September 2024,
Accepted 24th December 2024

DOI: 10.1039/d4bm01178c

rsc.li/biomaterials-science

Nanomedicine-based photothermal therapy (PTT) has been considered as an excellent alternative for treatment of tumor tissue due to its high therapeutic efficiency and controllable range. However, the overexpression of heat shock proteins (HSPs) during PTT and the hypoxic properties of the tumor microenvironment can lead to intracellular thermal resistance and reduce its effectiveness. Reactive oxygen species (ROS), followed by the application of chemodynamic therapy (CDT) and photodynamic therapy (PDT), can eliminate HSPs and overcome thermal resistance. High concentration H_2O_2 was used to catalyze oxygen production in the tumor microenvironment to improve the anaerobic state. Therefore, we present a multifunctional nanocarrier system driving chemodynamic–photodynamic–photothermal synergistic therapy *via* self-supplied hydrogen peroxide and relieved hypoxia for prostate tumor treatment.

1. Introduction

The incidence of prostate cancer is increasing year by year, and it has become a global male health issue. Worldwide, the incidence of prostate cancer ranks second among male malignant tumors.[1] In China, many prostate cancer patients are diagnosed at an advanced stage.[2] Treatments for advanced prostate cancer include androgen deprivation therapy, radiotherapy, chemotherapy, and more recently, immunotherapy.[3] However, these treatments have their limitations and often come with significant side effects. Hyperthermia can induce tumor cell death and enhance the efficacy of radiotherapy and chemotherapy. Raising the temperature of the tumor tissue to 40–43 °C can promote tumor cell apoptosis,[4] and when the temperature reaches 60 °C, it can achieve tumor tissue ablation.[5] Photothermal therapy (PTT) has emerged as a novel and effective treatment method, playing a significant role in the comprehensive treatment of various malignant tumors.[6] PTT is a non-invasive tumor treatment method in which photothermal materials convert light energy into heat to kill tumor cells under the irradiation of an external light source such as near-infrared light (NIR). As a new type of tumor treatment, PTT offers advantages such as non-invasiveness, high targeting specificity, and minimal side effects, showing great potential in the development of tumor therapies.[7]

During photothermal therapy, tumor cells may overexpress heat shock proteins in response to stress, leading to heat resistance and reduced therapeutic efficacy.[8,9] Previous studies have found that photodynamic therapy (PDT) and chemodynamic therapy (CDT) can generate a large amount of reactive oxygen species (ROS) within tumor cells, which in turn induce tumor cell apoptosis by activating related pathways through caspase apoptosis proteins.[10] Additionally, the production of ROS can reduce the expression of heat shock proteins, thereby weakening their heat resistance capabilities.[11] Photodynamic therapy utilizes photosensitizers that, under the irradiation of an external light source at a specific wavelength, convert molecular oxygen into cytotoxic reactive oxygen species (ROS) through photobiological reactions. This process disrupts the double-stranded DNA structure, causes lipid peroxidation of cell and mitochondrial membranes, and induces cell apoptosis.[12–15] Chemodynamic therapy leverages the catalytic

[a]*Shandong Provincial Third Hospital, Shandong University, Jinan, Shandong, 250031, P.R. China*
[b]*Qilu Hospital, Shandong, University, 107 Wenhua West Road, Lixia District, Jinan, Shandong, 250012, P.R. China. E-mail: shibenkangsdu@163.com, bkangshi@163.com*
[c]*School of Pharmaceutical Sciences, Key Laboratory for Natural Active Pharmaceutical Constituents Research in Universities of Shandong Province, Shandong Analysis and Test Center, Qilu University of Technology (Shandong Academy of Sciences), Jinan, Shandong, 250353, P.R. China. E-mail: yisheng_zhao@qlu.edu.cn*
[d]*Shandong Provincial Hospital Affiliated to Shandong First Medical University, Jinan 250021, P.R. China. E-mail: wonderfulwater1989@163.com*

† Electronic supplementary information (ESI) available. See DOI: https://doi.org/10.1039/d4bm01178c

properties of nanomaterials to generate large amounts of ROS through Fenton or Fenton-like reactions, thereby killing tumor cells and promoting tumor cell apoptosis.[16,17]

Although PDT and CDT can produce a large amount of reactive oxygen species (ROS) within tumor tissues, their effectiveness is limited by the unique tumor microenvironment, such as low pH, hypoxia, and high concentrations of glutathione.[18–21] These factors restrict the efficacy of PDT and CDT in practical applications. Previous studies have found that insufficient oxygen supply under external light irradiation significantly affects the efficacy of PDT, limiting ROS production and increasing tumor cell resistance to these standard treatment modalities.[22] Additionally, PDT generates ROS by consuming a large amount of oxygen in the tumor tissue, which exacerbates tumor hypoxia and significantly reduces the effectiveness of this approach. To improve the efficacy of PDT, many studies have focused on regulating the tumor microenvironment, increasing the oxygen content in tumor tissues, and reducing ROS metabolism.[23,24] Previous research has discovered that ascorbic acid (VC), a multifunctional reducing agent, is easily degraded within tumor cells, producing a large amount of hydrogen peroxide, which exerts ROS-induced tumor cell killing effects.[25–27] Studies have found that MnO_2 can not only catalyze the release of oxygen from excess hydrogen peroxide within tumor cells, alleviating tumor hypoxia, but also react with the overexpressed glutathione within tumor cells, reducing glutathione (GSH) consumption of ROS. In this process, the released Mn^{2+} can react with hydrogen peroxide in the tumor region to generate hydroxyl radicals, achieving auxiliary chemodynamic therapy.[28,29]

Here, we constructed a synergistic hollow mesoporous nanocomposite system containing manganese dioxide (MnO_2), a photosensitizer (IR825), and small molecule vitamin C (VC) (H-MnO_2@IR825-VC). This system improves the key issue of hypoxia within tumors by supplying hydrogen peroxide through the nanomaterials themselves, thereby enhancing chemodynamic therapy and photodynamic therapy to achieve synergistic photothermal, photodynamic, and chemodynamic treatment of tumors. Utilizing the catalytic properties of MnO_2, it can decompose the abundant H_2O_2 in the tumor microenvironment into oxygen, improving the hypoxic state within tumor cells.[30] Additionally, high heat generated under external near-infrared laser irradiation induces cell apoptosis and provides thermal stimulation for chemodynamic therapy to enhance its efficacy. Photodynamic and chemodynamic therapies generate more ROS, which can effectively regulate the expression of heat shock proteins within tumor cells, reducing their intracellular levels and eliminating heat resistance in tumor tissues during hyperthermia treatment, thereby enhancing the therapeutic efficacy. The increased temperature from photothermal therapy also strengthens the Fenton reaction, enhancing the efficacy of chemodynamic therapy and achieving the goal of multimodal combined therapy. This nanocomposite system, H-MnO_2@IR825-VC, overcomes the shortcomings of PTT, PDT, and CDT, while revealing the synergistic effects of these modalities.

2. Experimental section

2.1 Synthesis of hollow manganese dioxide nanocatalysts

The Stöber method[31] was employed for the synthesis of silica nanospheres in this investigation. Subsequently, the resulting SiO_2 precipitate (50 mg) was dispersed in water (50 mL) and gradually added dropwise to a potassium permanganate solution (6 g in 200 mL). After completing the addition under ultrasonic conditions, the reaction proceeded for an additional duration of 12 hours before centrifugation at a speed of 11 000 rpm for 30 minutes to collect the precipitate, which was subsequently washed with distilled water three times to obtain SiO_2@MnO_2 nanoparticles. This product was dissolved in a Na_2CO_3 aqueous solution (2 mol L^{-1}) and stirred at a temperature of 60 °C for another twelve hours to yield H-MnO_2 after high-speed centrifugation, followed by triple washing with distilled water and subsequent storage.

2.2 Preparation of H-MnO_2@VC

The hollow mesoporous H-MnO_2 was used to encapsulate small molecules of VC. Firstly, 15 mL (1 mg mL^{-1}) of $HMnO_2$ was lyophilized and then added to a solution of 10 mL (4 mg) VC (Beijing Solarbio Science & Technology Co., Ltd) and sonicated for 2 minutes. The mixture was then shaken overnight in the dark at room temperature (22 °C–24 °C), followed by washing and centrifugation with deionized water at 12 000 rpm for 10 minutes. Afterward, concentrated H-MnO_2@VC nanoparticles will be washed and diluted with an appropriate amount of pure water at a low temperature of 4 °C.

2.3 Preparation of H-MnO_2@IR825/VC

The photosensitizer IR825 was loaded onto the surface of the hollow mesoporous H-MnO_2@VC. Firstly, 5 mg IR825 (Shanghai Macklin Biochemical Technology Co., Ltd) was added with 10 ml DMSO (Beijing Solarbio Science & Technology Co., Ltd) and shaken until dissolved. 8 mg H-MnO_2@VC was weighed and added to the solution, and the mixture was continuously stirred by magnetic force for 24 hours at room temperature (22 °C–24 °C). The mixture was washed and centrifuged with double-distilled water at 12 000 rpm for 30 min. After washing, the concentrated H-MnO_2@IR825/VC nanoparticles were added with an appropriate amount of pure water and stored at 4 °C in the dark.

2.4 Characterization of H-MnO_2 and H-MnO_2@IR825/VC

Electron microscopy images were obtained using a transmission electron microscope (TEM, LIBRA 200 CS, Carl Zeiss Co., Germany) and a scanning electron microscope (SEM, Sigma, Carl Zeiss Co.). EDS (energy dispersive spectrometer) is used to analyze the types and contents of components of nanomaterials. X-ray photoelectron spectroscopy (XPS) (Thermo Scientific K-Alpha, USA) analysis was performed using an ESCALAB 250 X-ray photoelectron spectrometer equipped with a monochromatic X-ray source. Fourier transform-infrared spectra were obtained using a Thermo ls50 instrument (Thermo Fisher Scientific, Inc., MA, USA). Dynamic light scat-

tering (Zetasizer Nano Z; Malvern Instruments, Malvern, UK) was used to determine the hydrodynamic particle size distribution and zeta potential of the synthesized nanoparticles.

2.5 Oxygen generation properties of the nanoparticles

To investigate the oxygen generation performance of the nanoparticles, the oxygen concentration was measured every 1 min using a portable dissolved oxygen meter (WLDO-300, Shanghai Water Instrument Technology Co., Ltd). The oxygen electrode probe was placed in the reaction system containing H-MnO_2 and hydrogen peroxide, and the concentration of H-MnO_2 was set to 0, 50, 100 and 200 ppm, respectively. The temporal oxygen production curve was plotted.

2.6 Evaluation of the temperature elevation ability of H-MnO_2@IR825/VC

To evaluate the ability of H-MnO_2@IR825/VC to raise the temperature of the solution, the temperature rise of the nanomaterial under laser irradiation was recorded using an infrared thermographic camera (Ti32, Fluke) at a rate of 1 frame per second. The infrared thermograms obtained were analyzed using Analyze IR software.

To investigate the temperature increase of the materials under laser irradiation with respect to the concentration, the concentration of H-MnO_2@IR825/VC was set to 0, 50, 100, 200 and 500 ppm. Then, 100 μL of the H-MnO_2@IR825/VC solutions were placed in a 96-well plate, and the power density of the IR laser was set to 2 W cm^{-2}. Finally, the temperature increase was recorded and analyzed.

To investigate the correlation between the temperature increase and the laser density, 100 μL aliquots of a 100 ppm H-MnO_2@IR825/VC solution were placed in each well of a 96-well plate, and the laser power density was set to 1, 2, and 3 W cm^{-2}. The temperature increase was then recorded and analyzed.

To evaluate the stability of the photothermal conversion of H-MnO_2@IR825-VC, 100 μL aliquots of a 100 ppm H-MnO_2@IR825/VC solution were placed in each well of a 96-well plate and the laser density was set at 2 W cm^{-2}. Six cycles of IR laser irradiation were performed, each for 5 min, and the temperature increase of the nanoparticles under laser irradiation was recorded and analyzed.

2.7 Quantitative testing of H-MnO_2 loaded VC and IR825

VC solutions were prepared at concentrations of 5, 10, 20, 30, 40 and 50 μg mL^{-1} and their absorbance was measured to establish a standard curve. The H-MnO_2@IR825-VC materials were synthesized by adding 15 mg of H-MnO_2 and 4 mg of VC, which were then stirred overnight and centrifuged to obtain the precipitate. The absorbance of the remaining VC in the supernatant was measured and used to quantify the VC loading in the H-MnO_2@VC material.

IR825 solution was prepared at concentrations of 35, 40, 45, 50 and 62.5 μg mL^{-1}, and its absorbance was measured by using an ultraviolet spectrum spectrophotometer to establish the standard curve. H-MnO_2@IR825/VC material was synthesized by adding 8 mg H-MnO_2@VC and 5 mg IR825 followed by stirring overnight and centrifugation to obtain precipitates. The absorbance of the remaining IR825 in the supernatant was determined and used to determine IR825 loading in H-MnO_2@IR825/VC.

2.8 Photodynamic characteristics of the nanoparticles

To verify the photodynamic effect of the synthesized H-MnO_2@IR825/VC, the singlet oxygen production ability of the synthesized nanoparticles was analyzed by the commercial detection probe SOSG. The experimental group was tested using a SOSG kit with a fluorescence enzyme marker. Distilled water was used as a control. The concentration of the nanodrug in the experimental group was 200 ppm, and the concentrations of hydrogen peroxide were set as 0, 200, 500, and 1000 μM. Laser irradiation at a power of 1 W cm^{-2} was performed for 0, 1, 3, 6, 10, 15, 20, and 30 min.

2.9 Chemodynamic characteristics of H-MnO_2@IR825/VC

To investigate the ability of the synthesized nanomedicine platform to generate hydroxyl radicals, the experimental group was tested using the TMB kit. Appropriate temperature and PH values are required for CDT to play a therapeutic role. The optimal reaction temperature and PH were determined by detecting the results of different temperatures and pH values, and the experimental data were obtained by using fluorescence enzyme labeling.

A consistent reaction system was established when the concentration of H-MnO_2@IR825/VC was 200 ppm and the concentration of hydrogen peroxide was 500 μM. The reaction was carried out in a 37 °C water bath, and the pH values were taken as 4.0, 5.0, and 6.5 to investigate the optimal pH value of the reaction. To investigate the effect of temperature on hydroxyl radical generation, the reaction temperatures were set at 30, 37, 40 and 43 °C.

2.10 Cell culture

Human prostate cancer cells, PC3, were purchased from Shanghai Qi Da Biotechnology Co. (Shanghai, China). DMEM supplemented with 10% fetal bovine serum (FBS), streptomycin (100 μg mL^{-1}), and penicillin (100 μg mL^{-1}) was used as the culture medium. Cells were cultured at 37 °C under a 5% CO_2 atmosphere. The spent cell culture medium was replenished daily.

2.11 Cytotoxicity studies *in vitro*

To investigate the *in vitro* anti-tumor effects of PDT, PTT, CDT, and their synergistic effects, cell viability was measured using a CCK-8 assay kit (Meilun Biochemical Technology Co., Ltd). 1 × 105 PC3 cells were inoculated into each well of a 24-well culture plate containing 500 μL of culture medium. When the cells reached approximately 80% confluence, the spent cell culture medium was removed, and nanodrug culture medium was added.

The cells were then classified according to the planned experimental groups: Group 1, PBS (control); Group 2, PBS +

Laser; Group 3, H-MnO_2@IR825; Group 4, H-MnO_2@IR825 + Laser; Group 5, H-MnO_2@IR825-VC; and Group 6, H-MnO_2@IR825-VC + Laser. The cells with the nanodrug added were incubated in a 37 °C incubator for 24 h, and then the groups that required laser irradiation were irradiated at a density of 2 W cm^{-2} for 10 min. Cell viability was measured using a CCK-8 kit to verify the *in vitro* anti-tumor effect of each treatment.

To simulate the anoxic tumor microenvironment, the cells with the nanodrug added were incubated in a 37 °C, 5% O_2 hypoxic incubator. After replacing the cell culture medium, cell viability was measured using a CCK-8 assay kit, and the data were plotted accordingly.

2.12 *In vitro* intracellular uptake assay

To verify whether H-MnO_2@IR825-VC can enter cells, H-MnO_2@IR825-VC was combined with the fluorescent agent FITC. PC3 cells were cultured in 24-well plates and incubated in a 37 °C cell culture incubator for 24 h. The spent medium was then replaced with a fresh medium containing 200 ppm of H-MnO_2@IR825-VC, and the entry of the nanodrug into the cells was observed *via* laser confocal microscopy after 1, 3, 6, and 12 h.

2.13 Apoptosis assay

To analyze the *in vitro* anti-tumor effects of PDT, PTT and CDT, the survival and death of PC3 cells were visualized using a CAM/PI double-staining kit (Meilun Biochemical Technology Co., Ltd). The PC3 cells were inoculated in each well of a 24-well culture plate. When the cells reached approximately 80% confluency, the spent cell culture medium was removed, and nanodrug medium was added. The cells were then classified according to the planned experimental groups: Group 1, PBS; Group 2, PBS + Laser; Group 3, H-MnO_2@IR825; Group 4, H-MnO_2@IR825 + Laser; Group 5, H-MnO_2@IR825-VC; and Group 6, H-MnO_2@IR825-VC + Laser. The cells were incubated in a 37 °C incubator for 24 h, and the groups that required laser irradiation were irradiated at a laser density setting of 2 W cm^{-2} for 10 min. Finally, the cells were stained with a calcein AM/PI double-staining kit for 30 min and analyzed using fluorescence microscopy.

To quantitatively assess cell apoptosis in each experimental group, the apoptosis of PC3 cells was visualized using a PI/annexin V apoptosis detection kit (BD Biosciences Co., Ltd). The PC3 cells were inoculated in each well of a 24-well cell culture plate containing 500 μL culture medium. When the cells reached approximately 80% confluence, the spent cell culture medium was removed and nanodrug medium was added. The cells were then classified according to the planned experimental groups: Group 1, PBS (control); Group 2, PBS + Laser; Group 3, H-MnO_2@IR825; Group 4, H-MnO_2@IR825 + Laser; Group 5, H-MnO_2@IR825-VC; and Group 6, H-MnO_2@IR825-VC + Laser. The cells were incubated in a 37 °C incubator for 24 h and then the groups that required laser irradiation were irradiated at a laser density setting of 2 W cm^{-2} for 10 min. Finally, the cells were stained with a PI/annexin V apoptosis detection kit and analyzed using flow cytometry.

2.14 ROS production experiment based on PC3 cells

The production of reactive oxygen species in each group was analyzed using a reactive oxygen species detection kit (Meilun Biochemical Technology Co., Ltd). The PC3 cells were cultured in a 24-well plate. The experimental groups were designed as follows: Group 1, PBS; Group 2, PBS + Laser; Group 3, H-MnO_2@IR825; Group 4, H-MnO_2@IR825 + Laser; Group 5, H-MnO_2@IR825/VC; and Group 6, H-MnO_2@IR825/VC + Laser. When the cell confluence reached approximately 80%, the spent cell culture medium was removed and nanodrug medium was added. After 24 hours of incubation, the cell culture medium was replaced as per the experimental design. Then, the groups that required laser irradiation were irradiated at a laser density setting of 2 W cm^{-2} for 10 min. Reactive oxygen species (ROS) were stained using a reactive oxygen species detection kit, and the level of ROS production was observed using a fluorescence microscope.

In order to compare the therapeutic effects of photothermal therapy and photodynamic therapy in oxygen-rich and hypoxic environments, we simultaneously incubated the cells in a 37 °C, 5% O_2 hypoxic incubator to simulate the hypoxic microenvironment of tumor cells. After 12 hours of drug incubation, the cells were irradiated with an 825 nm laser for 10 minutes.

2.15 DNA damage in PC3 cells treated with H-MnO_2@IR825/VC nanoparticles

The effect of H-MnO_2@IR825/VC nanoparticles on the DNA damage of PC3 cells under laser irradiation was evaluated by using a DNA damage detection kit, and the DNA damage marker γ-H2AX (phosphorylated γ-H2AX) was detected by immunofluorescence staining. The PC3 cells were seeded in 24-well plates and incubated in a hypoxic incubator for 24 h, and then the cells were grouped as above. The cells added with nanomedicine were incubated in a hypoxic incubator for 12 h, and the cells in need of laser irradiation were irradiated with 2 W cm^2 power density for 10 min. The DNA damage of PC3 cells was observed under a fluorescence microscope.

2.16 Establishment of animal tumor models

To investigate the *in vivo* anti-tumor effects of PDT, PTT, CDT, and their synergistic effects, the nanodrug were injected in the nude mice with tumor.

Firstly, thirty-six healthy male BALB/c nude mice (6 weeks old) were purchased from Jinan Pengyue Experimental Animal Technology Co. and housed in the Experimental Animal Center of Shandong Provincial Third Hospital. All animal procedures were performed in accordance with the Guidelines for Care and Use of Laboratory Animals of Shandong University and approved by the Animal Ethics Committee of Shandong Provincial Third Hospital (No. DWKYLL-2022010).

Then, PC3 cells were cultured at 37 °C in a cell culture incubator. The cells of the cell culture flasks were suspended with an appropriate amount of trypsin solution (Gibco), and the

tumor cell suspension was centrifuged at 1000 rpm for 5 min, washed twice with PBS, and then resuspended in PBS. Next, 150 μL of the cell suspension (containing approximately 1×10^6 cells) was injected subcutaneously into the foreleg of the nude mice to establish a transplantation tumor model.

Finally, when the size of the tumor reached approximately 150 mm^3, the PC3 tumor-bearing nude mice were randomly assigned to six groups ($N = 6$ per group): Group 1: PBS; Group 2: H-MnO_2@IR825; Group 3: H-MnO_2@IR825-VC; Group 4: PBS + Laser; Group 5: H-MnO_2@IR825 + Laser; Group 6: H-MnO_2@IR825-VC + Laser. The nude mice belonging to different experimental groups received tail vein injections of PBS or nanodrug solution. The concentration of the injected solution was set at 200 ppm for all groups.

2.17 Body weight and tumor volume analysis in nude mice

The tumor volumes and weights of the nude mice were recorded and analyzed within 14 days after the treatment. The horizontal and vertical dimensions of the tumors were measured every other day using vernier calipers. The tumor volume was calculated as follows: volume = (horizontal length × vertical length^2)/2. Besides, the body weights of the nude mice were obtained every other day by weighing them on a scale.

2.18 *In vivo* photothermal characteristics of the nanoparticles

Twenty-four hours after injection, one nude mouse, each from groups 2 and 6. was taken and injected intraperitoneally using an anesthetic drug (tribromoethanol, 200 mg kg^{-1}) and irradiated with a laser at a density of 2 W cm^{-2} for 10 min. During this procedure, the temperature increase of the tumors under laser irradiation was recorded using an infrared thermographic camera (Ti32, Fluke) at a rate of 1 frame/second. The infrared thermograms were analyzed using Analyze IR software.

2.19 Histological evaluation

The ability of each group to produce ROS to inhibit heat shock protein expression was determined by detecting the expression of HSP70 and HSP90; the apoptotic pathway involved in each treatment group was determined by detecting the expression of caspase-3 and caspase-9. Apoptosis was detected in each group *via* TUNEL, PCNA, and HE staining to determine the mechanism of cell death in each treatment group.

According to the experimental groups: Group 1, PBS (control); Group 2, PBS + Laser; Group 3, H-MnO_2@IR825; Group 4, H-MnO_2@IR825 + Laser; Group 5, H-MnO_2@IR825-VC; and Group 6, H-MnO_2@IR825-VC + Laser, the corresponding solutions were injected into the mice *via* the tail vein, and each group was irradiated with a laser on the tumor at a laser density of 2 W cm^{-2} for 10 min. Two cycles of tail vein drug injection and laser treatment were performed for each mouse. Thirty minutes after irradiation, one mouse was selected for anesthesia and tumor tissues were taken, frozen, and preserved in liquid nitrogen to detect ROS production. Twenty-four hours after the end of irradiation, nude mice were anesthetized using tribromoethanol, and tumor specimens were collected and fixed in 4% paraformaldehyde for 24 h. The tumor specimens were then paraffin-embedded and sectioned at a thickness of 5 μm for immunofluorescence analysis of HSP70, HSP90, caspase-3, and caspase-9 expression; PCNA and TUNEL staining and HE staining.

In order to explore the mechanism of tumor apoptosis induced by nanomaterials, the protein expressions of caspase-3, caspase-9 and PCNA in the tumor tissues of different treatment groups were detected by western blotting. ACTIN was used as an internal reference to determine the relative changes of caspase-3, caspase-9 and PCNA expression levels.

In addition, in order to explore the inhibitory effect of ROS on the expression of heat shock proteins in tumor tissues, the expression of HSP70 and HSP90 proteins in the tumor tissues of nude mice in each group was detected by western blotting. ACTIN was used as an internal reference to determine the relative changes of HSP70 and HSP90 expression levels.

2.20 Biotoxicity testing of materials *in vivo*

At the end of the experiment, nude mice were anesthetized *via* intraperitoneal injection with tribromoethanol (200 mg kg^{-1}). The liver, kidneys, heart, and lungs were taken for HE testing to investigate whether the nanoparticles used in the experiment were biologically toxic to nude mice.

2.21 Statistical analysis

Statistical analysis was performed using SPSS 20 software. Significant differences were determined using one-way analysis of variance (ANOVA) and student's *t*-test. * denotes a *p*-value of <0.05 (significant result), ** denotes a *p*-value of <0.01 (very significant), and *** denotes a *p*-value of <0.001 (highly significant).

3. Results and discussion

3.1 Synthesis and characterization of H-MnO_2@IR825/VC

The morphology of the prepared nanoparticles was observed using TEM, as shown in Fig. 1A and Fig. S1.† The elemental composition of Mn and O (Fig. 1B and C) and C and N (Fig. S2 and S3†) in H-MnO_2@IR825/VC can also be observed *via* TEM. SEM imaging revealed that the morphology of H-MnO_2@IR825/VC was spherical and uniform, the size of H-MnO_2@IR825/VC was about 100 nm under an electron microscope, and hollow structures could be clearly seen. There was no effect of drug loading on the electropermeable morphology (Fig. 1D). EDS results show that H-MnO_2 successfully loaded VC and IR825 (Fig. 1E).

Based on the XPS spectrum, it was revealed that the peaks located at binding energies of 642.09 eV and 653.77 eV can be attributed to the Mn 2p3/2 and 2p1/2 signals of Mn^{2+} ions, respectively. The peaks at 642.77 eV and 654.09 eV correspond to the Mn^{4+} 2p3/2 and 2p1/2 signals, respectively. The results of XPS showed that VC and IR825 did not affect the structure of H-MnO_2, and H-MnO_2 still had its own properties. In

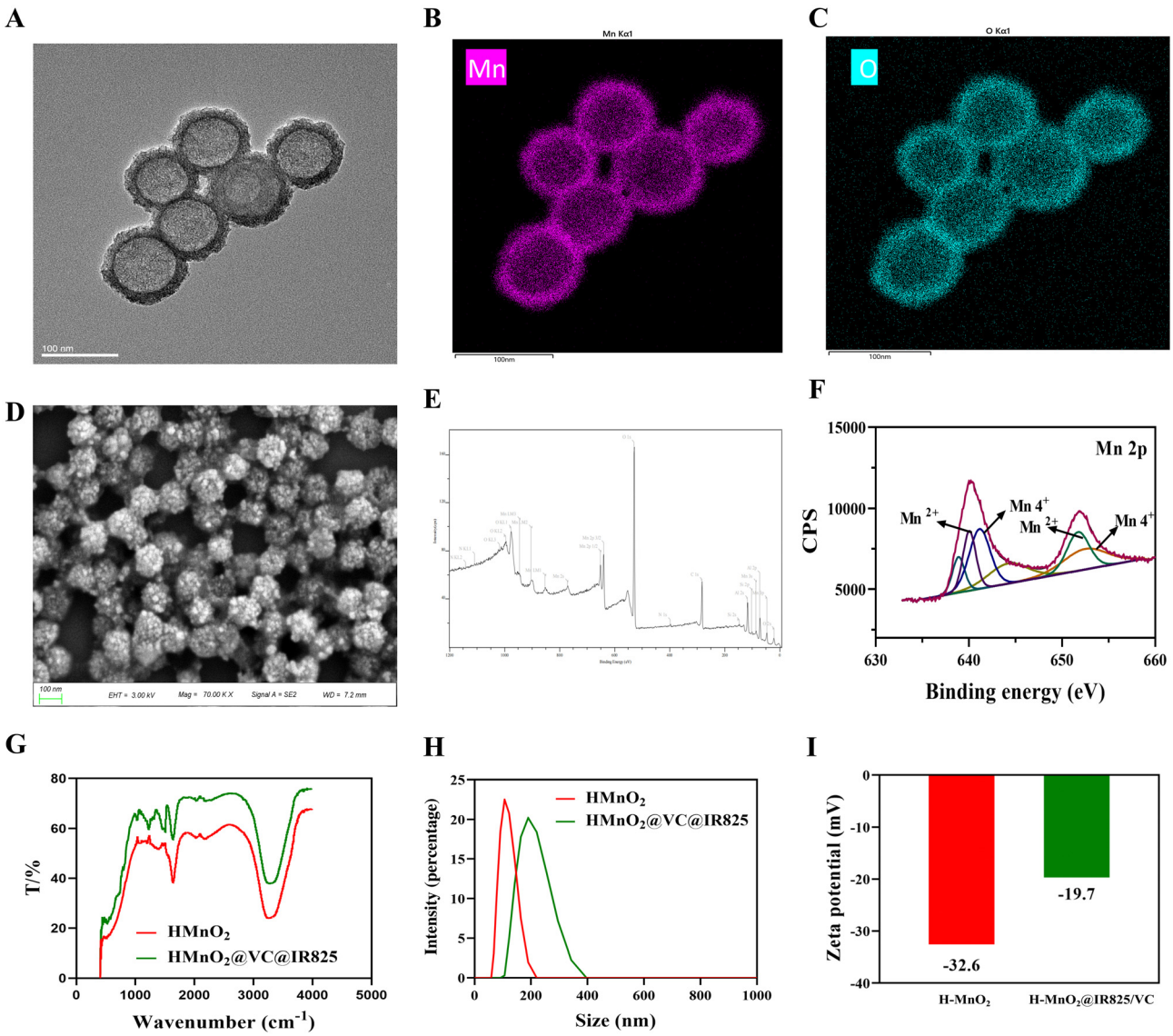

Fig. 1 Structural and physicochemical characterization of the H-MnO_2@IR825-VC particles. (A–C) TEM images. (D) SEM images. (E and F) XPS of the H-MnO_2@IR825-VC particles. (G) Fourier transform-infrared spectra of the H-MnO_2 and H-MnO_2@IR825-VC particles. (H) Particle size distribution of the nanoparticles. (I) Zeta potential of the nanoparticles.

addition, the results of the elemental spectrum showed that the Br peak was not detected in the sample H-MnO_2, while the Br orbital was detected in H-MnO_2@IR825/VC, indicating that VC and IR825 were successfully modified (Fig. 1F).

Based on the FTIR analysis results, we could observe the IR spectrum of H-MnO_2@IR825/VC, which clearly showed the absorption peaks at different wave numbers, and the IR spectrum of H-MnO_2 after loading IR825 and VC changed significantly, confirming the synthesis of the multifunctional nanoplatform drug H-MnO_2@IR825/VC in this experimental study (Fig. 1G). The hydrated particle size of H-MnO_2 was about 110 nm, and the hydrated particle size of H-MnO_2@IR825-VC was about 180 nm, The hydrated particle size results could prove the successful modification of IR825-VC (Fig. 1H). The zeta potential of H-MnO_2@IR825/VC was also examined, which was mainly at −19.7 mV, indicating that the particles had good stability in solution (Fig. 1I).

Based on the above results, IR825 and VC were successfully loaded in H-MnO_2.

3.2 Oxygen generation properties of the nanoparticles

To investigate the oxygen generation properties of the nanoparticles, oxygen concentrations were measured every 1 min using a portable dissolved oxygen meter. Distilled water was used as a control. To evaluate the ability of H-MnO_2 to catalyze the decomposition of H_2O_2 to produce O_2, the concentration of H-MnO_2 was set to 200 ppm. By adjusting the concentration of H_2O_2, a gradual increase in the solubility of oxygen in the solution was observed; a higher H_2O_2 concentration indicated a higher oxygen solubility level (Fig. 2A).

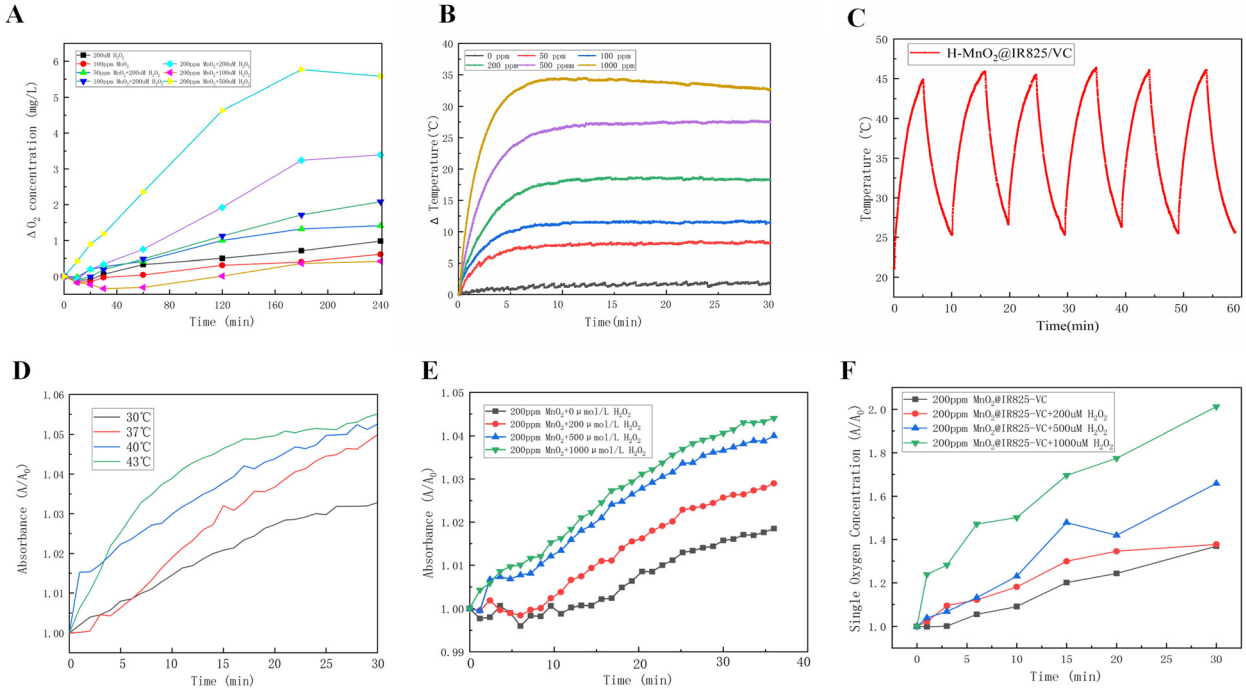

Fig. 2 Examination of the performance characteristics of the nanoparticles. (A) Curves showing the oxygen concentration with respect to time in an H-MnO_2 solution (200 ppm) containing H_2O_2 at concentrations of 0, 200, 500, and 1000 μM. (B) Curves of the temperature change with respect to time for an H-MnO_2@IR825-VC solution subjected to laser irradiation. The concentration of H-MnO_2@IR825-VC was set to 0, 50, 100, 200 and 500 ppm. (C) Verification of the photothermal stability of H-MnO_2@IR825-VC. The curve shows the change in the temperature of the H-MnO_2@IR825-VC solution with time by turning the laser switch on or off every 5 min, with 10 min as one cycle. (D) Time-course absorbance curves showing the amount of hydroxyl radicals produced by the reaction of H-MnO_2@IR825-VC (200 ppm) and H_2O_2 (500 μM) at a pH level of 5.0 and varying temperatures: 30, 37, 40 and 43 °C. (E) Time-course absorbance curves showing the amount of hydroxyl radicals produced by the reaction of H-MnO_2@IR825-VC (200 ppm) containing H_2O_2 at concentrations of 0, 200, 500, and 1000 μM. (F) When exposed to laser irradiation, time-course absorbance curves showing singlet oxygen produced by the reaction of H-MnO_2@IR825-VC (200 ppm) containing H_2O_2 at concentrations of 0, 200, 500, and 1000 μM.

The result shows that H-MnO_2 has catalase-like activity, which can catalyze the decomposition of H_2O_2 to produce O_2 and increase the solubility of oxygen in water.

3.3 Photothermal characteristics of the nanoparticles

To evaluate the ability of H-MnO_2@IR825-VC to raise the temperature of a solution, H-MnO_2@IR825-VC was diluted to 0, 50, 100, 200 and 500 ppm in a 96-well plate, and the power density of the infrared laser was set to 2 W cm^{-2}. The result showed that with an increase in the H-MnO_2@IR825-VC concentration, the temperature gradually increased, and reached a peak within 10 min. The temperature gradually stabilized thereafter (Fig. 2B).

Fig. S6† shows that when the concentration of H-MnO_2@IR825-VC was diluted to 100 ppm and placed in a 96-well plate, the temperature of the reaction solution increased with increasing laser power density.

To evaluate the photothermal stability of H-MnO_2@IR825-VC, the concentration of H-MnO_2@IR825-VC was diluted to 100 ppm and placed in a 96-well plate. The infrared thermogram was analyzed by using Analyze IR software to determine the photothermal stability of the nanodrugs. According to the data, six experimental cycles were performed, with the laser density set at 2 W cm^{-2}, and each cycle was run for 10 min (5 min with irradiation and 5 min without irradiation). The solution reached a similar peak temperature in each cycle (Fig. 2C). The experimental results confirm that H-MnO_2@IR825-VC is a relatively stable photothermal conversion agent.

3.4 Quantitative testing of H-MnO_2 loaded VC and IR825

The standard curve was constructed by plotting the absorbance of the solution measured using an ultraviolet spectrophotometer against the corresponding VC concentrations, as shown in the graph (Fig. S7B and S8A†). By measuring the absorbance of the supernatant obtained after the preparation of H-MnO_2@VC and using the standard curve, the mass of VC in the supernatant was calculated, and the loading efficiency of H-MnO_2 for VC was determined. By detecting that the OD value of the H-MnO_2@VC sample solution was 0.362, the concentration was calculated as 7 μg mL^{-1} and the total volume was 10 mL. The amount of VC in the supernatant was 70 μg, and the total amount added was 4 mg, so the amount of drug modification was 3.93 mg.

The standard curve was constructed by plotting the absorbance of the solution measured using an ultraviolet spectro-

photometer against the corresponding IR825 concentrations, as shown in the graph (Fig. S7A and S8B†). By detecting that the OD value of the supernatant of our synthesized H-MnO_2@IR825/VC sample solution was 3.23, the concentration of IR825 in the supernatant was calculated to be 28.07 μg mL^{-1}. The total volume of the solution we prepared was 10 mL, and the content of IR825 in the supernatant was calculated to be 280.7 μg. When the total amount of IR825 added to the prepared sample was 5 mg, the drug loading of IR825 on the prepared H-MnO_2@IR825/VC nanoparticles was 4.7193 mg.

At the same time, the ultraviolet spectra of H-MnO_2 and H-MnO_2@IR825/VC nanoparticles were detected. The results showed that IR825 and VC were successfully loaded on H-MnO_2, and there was no mutual interference between them, as shown in Fig. S7C and D.†

3.5 Chemodynamic characteristics of the nanoparticles

To investigate the ability of the synthesized H-MnO_2@IR825-VC to generate hydroxyl radicals, a TMB hydroxyl radical detection kit was used to explore the optimal reaction temperature and the optimum reaction PH.

Different reaction temperatures were set: 30, 37, 40 and 43 °C. The hydroxyl radical content generated in the reaction system with 200 ppm nanoparticles and hydrogen peroxide was measured using a commercially available TMB hydroxyl radical detection kit. The result revealed that the highest hydroxyl radical content was generated at 43 °C (Fig. 2D).

The hydroxyl radical content generated in the reaction system with 200 ppm nanoparticles and different concentrations of hydrogen peroxide was measured using a commercially available TMB hydroxyl radical detection kit. Different concentrations of hydrogen peroxide were set: 0, 200, 500 and 1000 μmol L^{-1}. By adjusting the concentration of H_2O_2, the more hydroxyl radicals were produced (Fig. 2E).

Reactions with different pH values were set (4.0, 5.0, and 6.5), and the hydroxyl radical content generated in each reaction system containing 200 ppm nanoparticles and hydrogen peroxide was measured using a commercially available TMB hydroxyl radical detection kit. The result revealed that the amount of hydroxyl radicals generated was the highest at a pH of 4.0 (Fig. S9†). The result suggests that the acidic tumor microenvironment favors ROS production, which induces tumor cell apoptosis.

Collectively, these results demonstrated that our NPs were appropriate candidates for self-supplying *in situ* oxygen generation, and then providing substrates for the reactions mediated by PDT and CDT.

3.6 Photodynamic characteristics of the nanoparticles

To verify that the synthesized nanosystem can mediate PDT and generate singlet oxygen species, the experimental group was tested using a SOSG kit with a fluorescence enzyme marker. Compared with distilled water, H-MnO_2@IR825-VC mixed with hydrogen peroxide showed a markedly enhanced singlet oxygen generation ability when exposed to laser irradiation for 0, 1, 3, 6, 10, 15, 20, and 30 min. The result reveals that the synthesized nanosystem could catalyze the decomposition of H_2O_2 to produce O_2 and the presence of photosensitizers could catalyze O_2 to generate singlet oxygen species (Fig. 2F). H-MnO_2@IR825-VC generates singlet oxygen *via* photodynamic therapy under laser light using the oxygen available within the reaction system. As a whole, these results demonstrated that H-MnO_2@IR825-VC could effectively generate singlet oxygen under light irradiation and serve as an efficient photodynamic agent.

3.7 Cytotoxicity studies *in vitro*

To investigate the *in vitro* anti-tumor effects of PDT, PTT, CDT, and their synergistic effects, cell viability was measured using a CCK-8 assay kit (Meilun Biochemical Technology Co., Ltd). The PBS group and PBS + Laser group served as a control. Compared with the control groups, the cell viability of all experimental groups was lower, with the H-MnO_2@IR825-VC + Laser group having the lowest cell viability (Fig. 3A). Similarly, we tested the cell viability using a CCK-8 detection kit in an anaerobic incubator. To simulate the anoxic tumor microenvironment, the PC3 cells with the nanodrug were incubated in a 37 °C anaerobic incubator. Compared with the PBS group and PBS + Laser group, the cell viability of all experimental groups was lower, with the H-MnO_2@IR825-VC + Laser group having the lowest cell viability (Fig. S10†). Thus, the PDT, PTT, and CDT effects studied in this project were proven to be effective in tumor cell killing and had a synergistic effect upon each other.

3.8 *In vitro* intracellular uptake studies

To verify whether the synthesized nanoparticles could enter into cells to exert therapeutic effects, fluorescein FITC was loaded on the surface of the synthesized nanoparticles to observe the phagocytosis of cells. Fluorescein isothiocyanate (FITC) 0.1 mg was weighed and dissolved in 0.1 mL DMSO, and 0.1 mL of the above solution was added to 5 mL H-MnO_2@IR825-VC (200 ppm) and nanosuspensions were obtained by sonication in the dark for 30 min at room temperature. H-MnO_2@IR825-VC/FITC was mixed into complete DMEM, and this culture medium was used to culture PC3 cells for 1, 3, 6 and 12 h. Observation using a fluorescence microscope showed that the material could enter the cytoplasm and that the nanoparticles which were swallowed into the cell gradually increased with time (Fig. S11†). These results show that the newly synthesized multifunctional nanomaterial H-MnO_2@IR825-VC can be phagocytosed by cells and be useful as an anti-tumor therapy. In addition, the results showed that the nanoparticles were not cytotoxic to PC3 cells.

3.9 Apoptosis assay

To analyze the *in vitro* anti-tumor effects of PDT, PTT and CDT, the survival and death of PC3 cells were visualized using a CAM/PI double-staining kit (Meilun Biochemical Technology Co., Ltd). The PC3 cells were inoculated in each well of a 24-well culture plate and observed using fluorescence

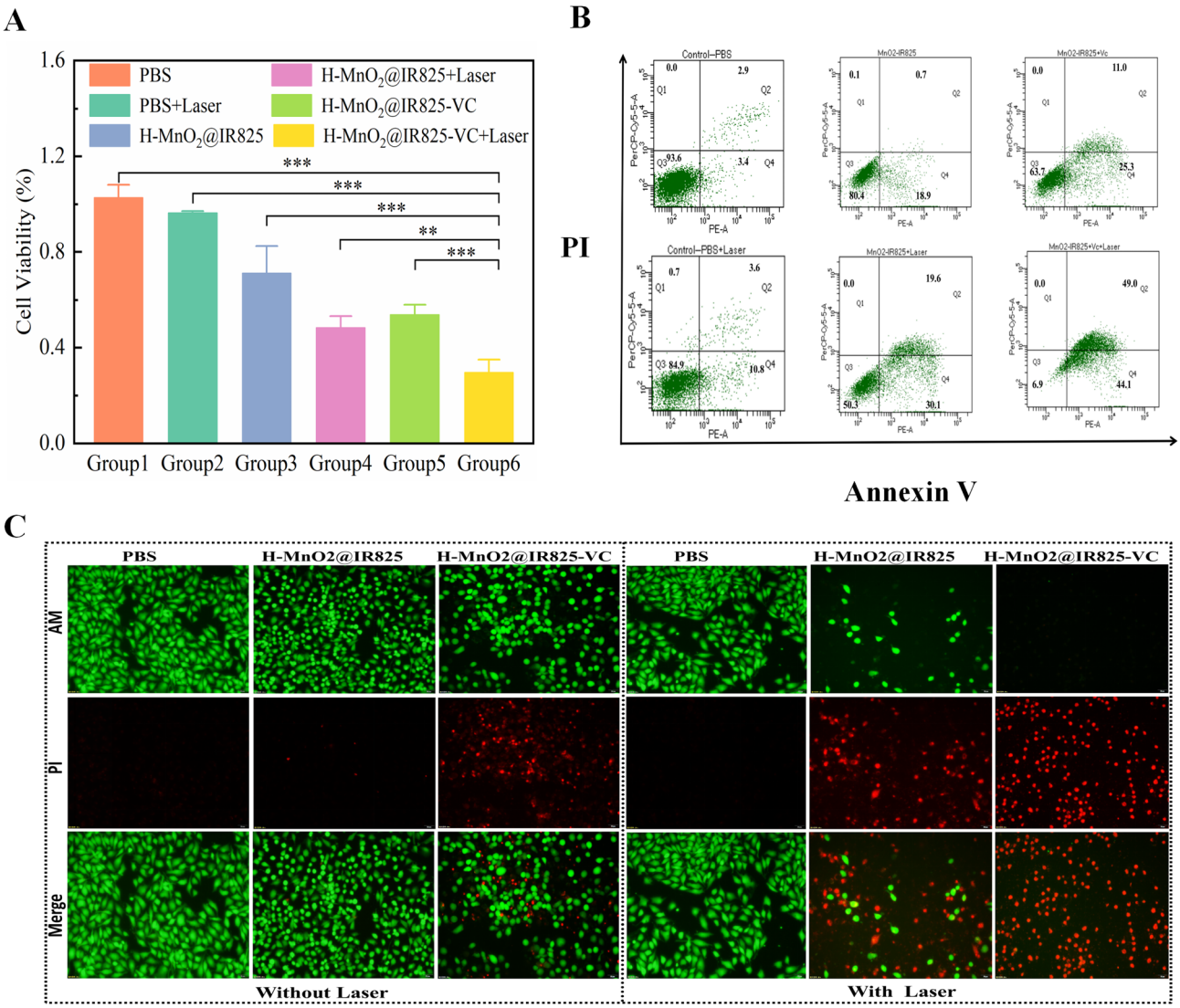

Fig. 3 Examination of the anti-tumor properties of the synthesized nanoparticles against prostate carcinoma PC3 cells. (A) Measurement of cell activity in each experimental group. (B) Quantitative analysis of cell apoptosis rates after annexin V/PI staining of PC3 cells from each experimental group. (C) PC3 cell survival status analysis in each experimental group after CAM/PI staining.

microscopy. Group 6, which was treated with H-MnO_2@IR825-VC + Laser, typically showed an apoptotic state and had significantly more apoptotic cells than the other groups. Compared with the PBS group and PBS + Laser group, the other groups had different degrees of apoptotic tumor cells (Fig. 3C). This result shows that the nanodrug *via* PTT, PDT, and CDT could effectively mediate the apoptosis of tumor cells.

3.10 Quantitative apoptosis assay

To quantitatively assess the cell apoptosis in each experimental group, the apoptosis of PC3 cells were visualized using a PI/annexin V apoptosis detection kit (BD Biosciences Co., Ltd). In the control group (Group 1), only 7.3% were apoptotic, indicating that the cells were in a good growth state. The apoptosis rates in Groups 2–5 were 14.4%, 19.6%, 49.7%, and 36.3%, respectively, showing relatively more evident apoptosis after treatment. The apoptosis rate of the cells in Group 6 reached as high as 93.1% after treatment, showing that the synergistic effect in this study has a strong ability to induce apoptosis in tumor cells (Fig. 3B and Fig. S12†).

3.11 ROS production experiment based on PC3 cells

The production of reactive oxygen species in each group was analyzed using a reactive oxygen species detection kit (Meilun Biochemical Technology Co., Ltd). The PC3 cells were cultured in a 24-well plate and the fluorescence intensity of ROS was observed under a fluorescence microscope. The figures show that, under normoxia, the PBS group exhibits the weakest fluorescence intensity and the H-MnO_2@IR825-VC + Laser group exhibits the strongest fluorescence intensity (Fig. 4A). Fig. 4B shows that under hypoxic conditions, H-MnO_2 can catalyze the production of a large amount of oxygen through the self-

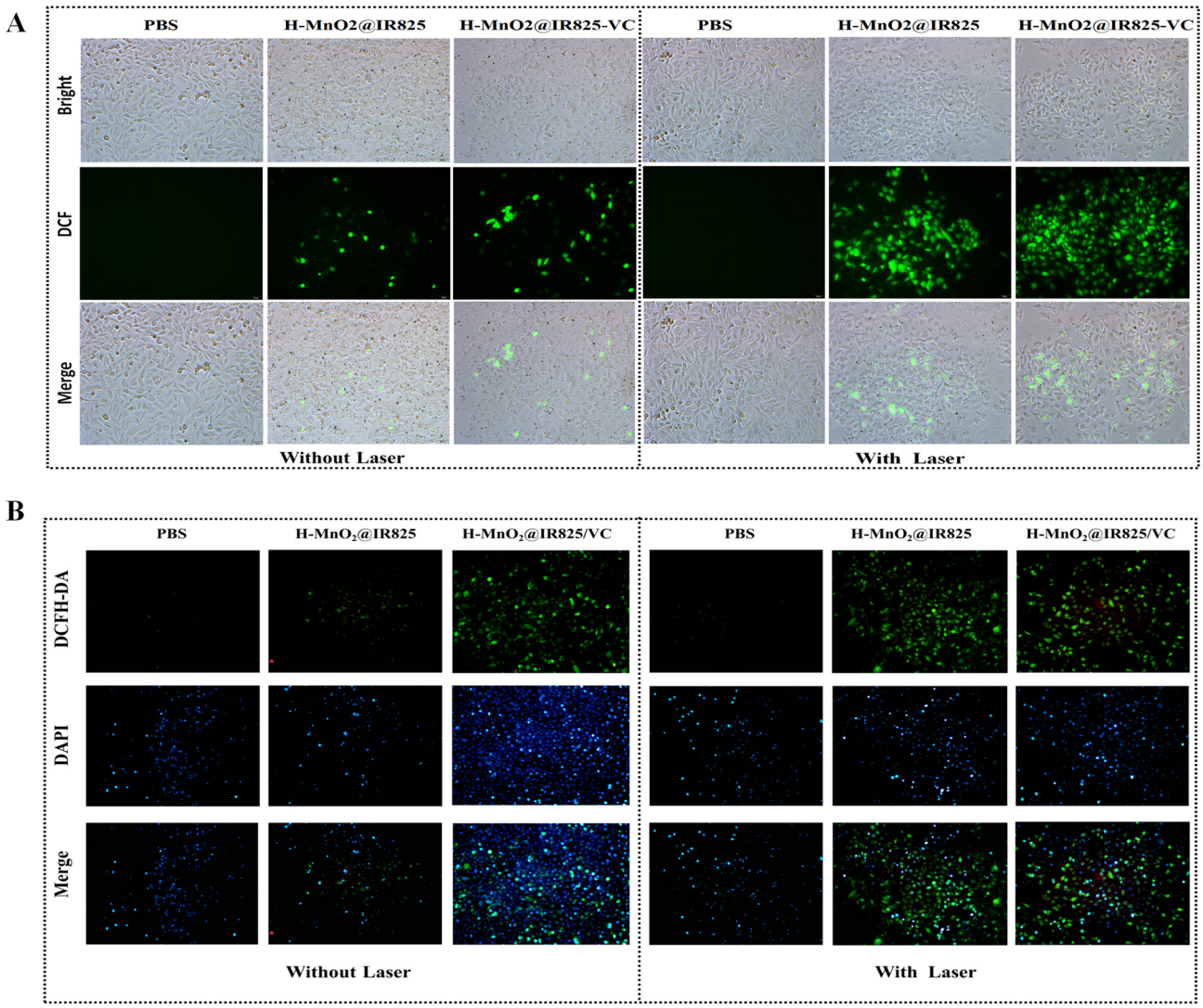

Fig. 4 *In vitro* experiment to detect the content of ROS generation at the cellular level. (A) Levels of reactive oxygen species (ROS) production in PC3 cells under normoxia in response to nanomedicine. (B) Levels of reactive oxygen species (ROS) production in PC3 cells under hypoxia and under nanomedicine treatment.

supply of hydrogen peroxide by VC, improve the hypoxic state of the tumor microenvironment, and promote CDT and PDT to produce a large amount of ROS. This reveals that the combination therapy of PTT, PDT, and CDT represented by H-MnO_2@IR825-VC + Laser generates the highest level of ROS, contributing to the inhibitory effect on tumor cells.

3.12 DNA damage in PC3 cells treated with H-MnO_2@IR825/VC nanoparticles

The effect of H-MnO_2@IR825/VC nanoparticles on the DNA damage of PC3 cells under laser irradiation was evaluated by using a DNA damage detection kit, and the DNA damage of each group was observed under a fluorescence microscope. Reactive oxygen species (ROS), as DNA damage factors, can increase tumor genomic instability and cause cell apoptosis. PC3 cells were incubated in a hypoxic incubator to mimic the hypoxic characteristics of the tumor microenvironment. Fig. 5 results show that the green fluorescence intensity of the control group treated with PBS was the weakest. In contrast, the green fluorescence intensity of H-MnO_2@IR825-VC nanoparticles was significantly enhanced under laser irradiation, which indicated that this group still produced a large amount of ROS under hypoxia, leading to DNA damage in tumor cells and exerting its anti-tumor effect.

3.13 *In vivo* anti-cancer efficacy of H-MnO_2@IR825-VC as a combination of PTT, PDT, and CDT

When the size of the tumor reached approximately 150 mm^3, the PC3 tumor-bearing nude mice were randomly assigned to six groups (n = 6 per group) and injected through their tail vein with 50 μL of the following treatment solutions: PBS (control), H-MnO_2@IR825 or H-MnO_2@IR825-VC (Group 1: PBS; Group 2: H-MnO_2@IR825; Group 3: H-MnO_2@IR825-VC; Group 4: PBS + Laser; Group 5: H-MnO_2@IR825 + Laser; Group

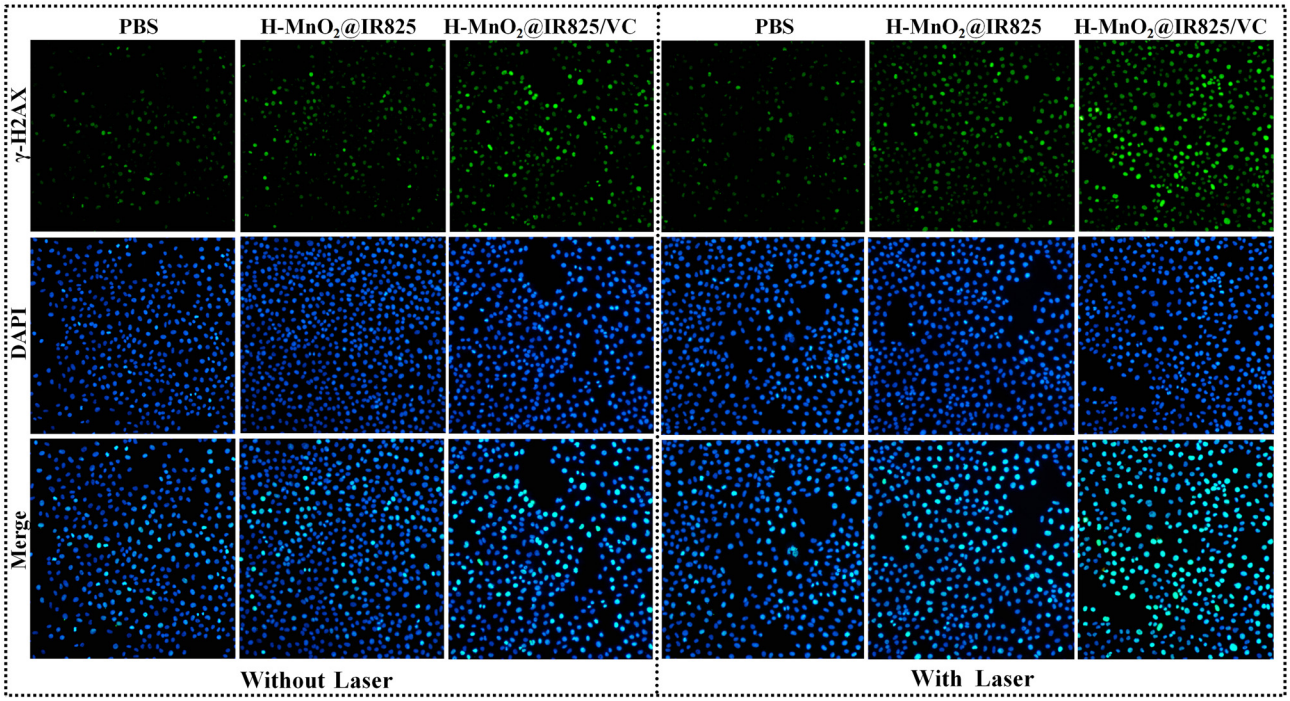

Fig. 5 DNA damage in PC3 cells treated with H-MnO_2@IR825/VC nanoparticles.

6: H-MnO_2@IR825-VC + Laser). The concentration of the injected solution was set at 200 ppm for all groups. At 24 h, after drug injection, the animals in each group were anesthetized with pentobarbital sodium and subjected to laser irradiation treatment at a laser power density of 2 W cm^{-2}. The animal experiment was conducted at the Laboratory Animal Research Center of Shandong Provincial Third Hospital with approval by the Ethical Committee of Shandong Provincial Third Hospital. In the process of animal experimentation, strict adherence to the "3R" principles, which advocate replacement, reduction, and refinement, should be strictly followed.

3.14 Changes in the body weight and tumor volume in nude mice

The therapeutic effects of the nanoparticles were also examined *in vivo*. To this end, the tumor volume was monitored over 14 days following the administration of the different treatments. The mice in the drug treatment groups exhibited smaller tumor growth than the PBS-treated control group, indicating that PTT, PDT, and CDT can all inhibit tumor growth.

The mice in the H-MnO_2@IR825-VC + Laser group (Group 6) had the smallest tumor volumes compared to all other groups (Fig. 6A, E and Fig. S13†). These results show that treatment with H-MnO_2@IR825-VC + Laser exhibited the most effective tumor growth suppression, which was attributed to the synergistic combination of PTT, PDT, and CDT.

During the treatment, body weight measurements for each group of animals were taken every other day. At the end of this experiment, no statistical difference was found between the weights of the animals across groups and the changes in the weight of the animals in each group (Fig. 6B). This reveals that H-MnO_2@IR825-VC has no evident toxic effects on the animals.

3.15 *In vivo* photothermal characteristics of the nanoparticles

To investigate the photothermal effect of H-MnO_2@IR825-VC on PC3 tumor-bearing mice, variations in the tumor temperature were recorded over time using an infrared thermographic camera. The maximum tumor temperature in the H-MnO_2@IR825-VC + Laser groups increased rapidly and ascended by about 10 °C; this indicates that nanoparticles are distributed within animal tumors and mediate PTT to produce high temperatures. By comparison, the temperature of the PBS group only increased slightly (Fig. 6C and D). The results suggests that the therapeutic effect of PTT is achieved by inducing apoptosis of tumor cells and inhibiting tumor growth through laser irradiation.

3.16 Evaluation of the apoptosis mechanisms *in vivo*

TUNEL, PCNA and HE staining were used to detect apoptosis in each group, and the mechanism of cell death in each treatment group was investigated.

Each group of nude mice received the corresponding treatment. After the end of the 14-day treatment, the mice were anesthetized and then sampled by sectioning the tumor tissues from each experimental group and by staining the sections for caspase-3 and caspase-9. The apoptotic pathways involved in each treatment group were determined by detect-

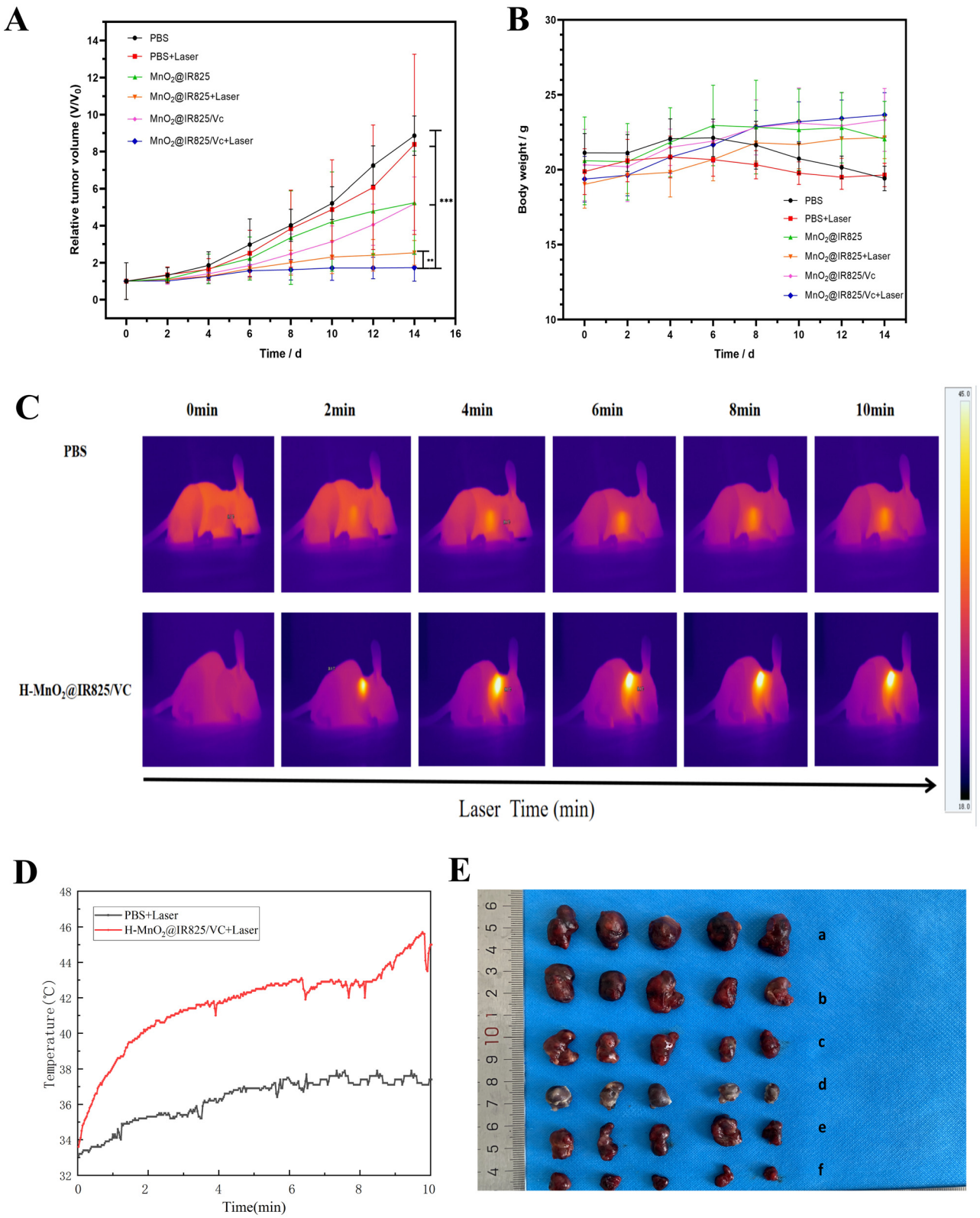

Fig. 6 *In vivo* anti-tumor studies (A) Curves showing the time-course changes in the subcutaneous tumor volume of the nude mice in each experimental group after treatment. (B) The changes in the body weight of the nude mice in each experimental group after treatment. (C) Thermal images of the body surfaces of the nude mice during laser irradiation, as recorded using a thermal infrared camera. (D) Curves showing the temperature change in the body surface of the nude mice under laser irradiation, as recorded using a thermal infrared camera. (E) Appearance of the subcutaneous tumors isolated from the nude mice: (a) PBS; (b) PBS + Laser; (c) H-MnO_2@IR825; (d) H-MnO_2@IR825 + Laser; (e) H-MnO_2@IR825-VC; and (f) H-MnO_2@IR825-VC + Laser.

ing the expression of caspase-3 and caspase-9. In the H-MnO_2@IR825-VC + Laser group, the expressions of caspase-3 and caspase-9 were the most obvious, and the cytoplasm showed strong brown staining. In contrast, the control group showed much lower expression levels (Fig. 7A and B). The overexpression of caspase-9 and caspase-3 in the H-MnO_2@IR825-VC + Laser group suggests that the apoptosis of tumor cells upon treatment with H-MnO_2@IR825-VC after laser irradiation was mediated by the caspase pathway. PCNA staining were used to detect apoptosis in each group, and the mechanism of cell death in each treatment group was investigated. The staining results showed that Group H-MnO_2@IR825-VC + Laser had

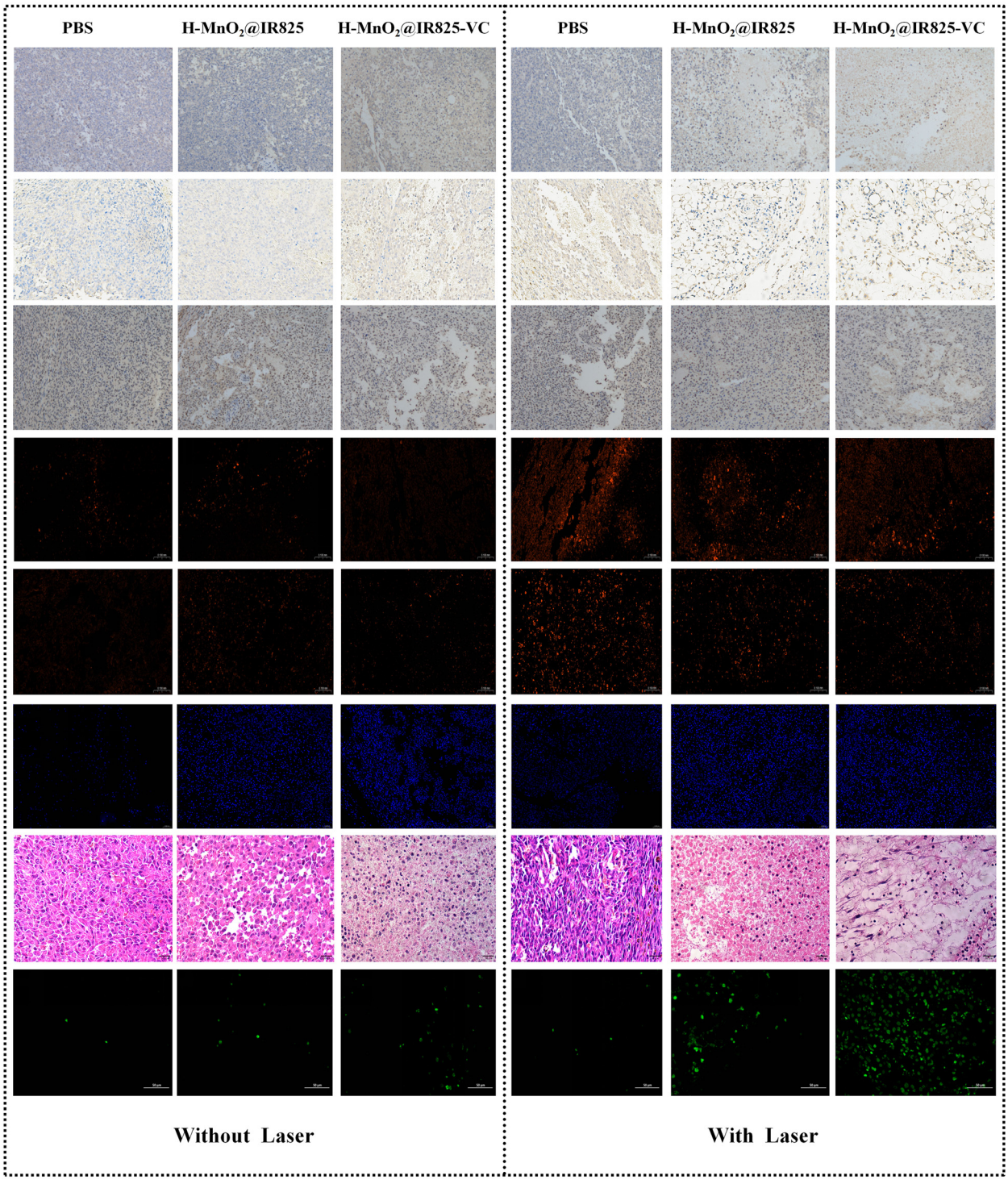

Fig. 7 Representative images of the stained tumor tissue sections of the nude mice after treatment in each experimental group. Each set of images was stained for (A) caspase-3, (B) caspase-9, (C) PCNA, (D) HSP70, (E) HSP90, (F) ROS, (G) HE and (H) TUNEL assays.

the lowest cell proliferation activity, while Group PBS and Group PBS + Laser had the highest proliferation activity. These results suggest that the nanoparticles have an inhibitory effect on the proliferation of tumor tissues (Fig. 7C).

Caspase-3 and caspase-9 are proteases that play a key role in the process of apoptosis and belong to the caspase family. Caspase-3 plays a central role in the execution phase of apoptosis and is able to cleave and inactivate a variety of key proteins, thereby triggering apoptosis. Caspase-3 is cleaved into two fragments with molecular weights of 17 kDa (p17) and 12 kDa (p12) and translocated to the nucleus during apoptosis. Cleaved caspase-3 activates caspase-6, caspase-7, and caspase-9 to form an apoptotic cascade. Caspase-9 belongs to the initiator of apoptosis, which can self-activate or mutually activate with the assistance of the corresponding proteins, recognize and activate downstream caspases, and cause a cascade reaction, eventually leading to cell apoptosis. Western blot results showed that the levels of caspase-3 and caspase-9 proteins were significantly increased in the tumor tissues of nude mice treated with the H-MnO_2@IR825/VC nanodrug combined with a laser compared with those in the PBS treatment group. These results indicate that H-MnO_2@IR825/VC can up-regulate the expression levels of caspase-3 and caspase-9 proteins, leading to the apoptosis of tumor cells and playing an anti-tumor role (Fig. 8A).

PCNA is a protein closely related to DNA synthesis, and its expression is significantly increased in tumor cells during cell division. Western blot results showed that the protein level of PCNA in the tumor tissue of nude mice in the H-MnO_2@IR825/VC nanotreatment group was significantly lower than that in the PBS treatment group, indicating that H-MnO_2@IR825/VC can significantly inhibit the division and proliferation of tumor cells and play an anti-tumor role under laser irradiation (Fig. 8B).

3.17 Evaluation of heat shock protein production

The expression of HSP70 and HSP90 was detected to determine the ability of cells in each group to produce ROS and inhibit the expression of heat shock protein. Immunofluorescence staining for HSP70 and HSP90 was performed to investigate the inhibitory effect of these ROS-generating therapies on the expression of heat-resistant proteins. The levels of heat shock proteins in Group H-MnO_2@IR825-VC + Laser were the lowest among all groups, while the highest levels were found in Group PBS + Laser (Fig. 7D and E). The overexpression of heat shock proteins (HSPs) during PTT can lead to intracellular thermal resistance and reduce its effectiveness. After laser irradiation, the different expressions of HSP70 and HSP90 show that the ROS produced by PDT and CDT can inhibit the production of heat shock proteins, thus reducing the heat resistance of tumor cells during PTT.

Western blot results showed that the expression of heat shock proteins was significantly decreased in the nude mice treated with H-MnO_2@IR825/VC nanoparticles, while the expression of HSP 70 and HSP 90 proteins was significantly increased in the PBS treatment group, which further proved that ROS inhibited the expression of heat shock proteins (Fig. 8B).

3.18 Assessment of ROS production

After receiving the corresponding nanodrugs and laser irradiation in each group of nude mice, tumor tissues were taken under anesthesia within 30 min and immediately preserved in liquid nitrogen to detect ROS production. ROS assays showed that the H-MnO_2@IR825-VC + Laser group had the highest ROS content, which was inseparable from the effect of PDT, CDT, and PTT-mediated temperature increase, all of which promoted ROS production (Fig. 7F).

3.19 Evaluation of apoptosis *in vivo*

Each group of nude mice was injected with the corresponding nanomedicines through the tail vein, and laser irradiation was performed for two treatment cycles. At 24 h, after the end of the treatment, the nude mice were anesthetized and harvested. Tissue sections were taken from each mouse for HE and TUNEL staining. The results showed that the tumor cells in PBS group and PBS + Laser group grew well. Compared with the PBS group, the H-MnO_2@IR825-VC + Laser group showed obvious apoptosis in the tumor tissue. In addition, different

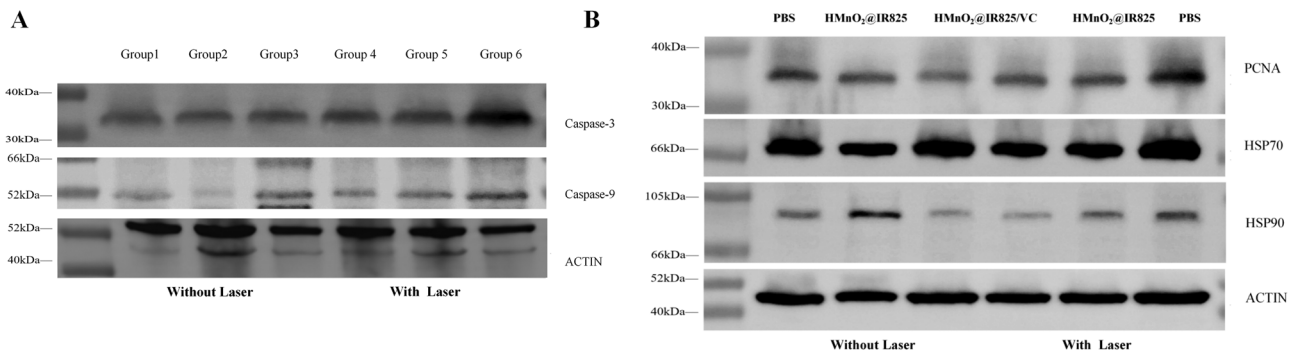

Fig. 8 Results of PCNA protein and HSP protein expressions in tumor tissues from different treatment groups. (A) Protein expression levels of caspase-3 and caspase-9 in the animal tumor tissues (Group 1: PBS; Group 2: H-MnO_2@IR825; Group 3: H-MnO_2@IR825-VC; Group 4: PBS + Laser; Group 5: H-MnO_2@IR825 + Laser; Group 6: H-MnO_2@IR825-VC + Laser). (B) Protein expression levels of HSP70 HSP90 and PCNA in the animal tumor tissues.

degrees of apoptosis were observed in the other groups, as shown in the photographic images of stained tissues (Fig. 7G).

Tumor tissues were isolated, sectioned, and stained, and cell proliferation was assessed. The results showed that the H-MnO_2@IR825-VC + Laser group had the worst state of tumor cells, the PBS group and the PBS + Laser group had the best state of tumor cell growth, and the remaining groups showed different degrees of growth inhibition (Fig. 7H). In conclusion, nanomaterial-mediated apoptosis of tumor cells was achieved, and there was a certain degree of synergy between multiple treatment modalities.

3.20 Biotoxicity testing of the nanoparticles *in vivo*

After formaldehyde fixation, the heart, lung, spleen, liver and kidney tissues of nude mice were sectioned and stained with HE. The results showed that there was no significant difference in the organs between the experimental group and the control group (Fig. S14†). The results revealed that the nanoparticles synthesized in this experiment had no obvious toxic effect on the organs of the animals.

4. Conclusions

In this study, we successfully optimized the formulation of a nanoplatform and synthesized a novel multifunctional nanoparticle composite H-MnO_2@IR825-VC. The nanocomposites significantly improve the hypoxic state of the tumor microenvironment and exhibit enhanced photothermal therapy, photodynamic therapy, and chemodynamic therapy capabilities. Through oxygen production and ROS production, the goals of HSP lysis and coupled thermal resistance were achieved, resulting in the inhibition of tumor growth and satisfactory therapeutic effects. This study presents a multifunctional nanoplatform for efficient prostatic carcinoma treatment *via* modulating ROS and HSPs. In summary, the present study provides an attractive strategy for the cleavage of thermal resistance and a novel adjunct and enhancement of heat-related therapies.

5. Methods and results

We developed a hollow nanocarrier system composed of near infrared (NIR)-light responsive heptamethine cyanines (IR825) and vitamin C(VC)-loaded hollow manganese dioxide nanocatalysts (MnO_2) to perform photothermal–chemodynamic–photodynamic synergistic therapy for tumor treatment. Mn^{2+} present in MnO_2 contributed to ROS generation *via* the Fenton reaction, inducing cell apoptosis by chemodynamic action. The effect of chemodynamic therapy (CDT) was enhanced through the conditions created by increased PTT-related temperature, VC-mediated hydrogen peroxide (H_2O_2) accumulation, and elevated tumor microenvironment acidity. The hollow manganese dioxide nanocatalysts possess nanozyme activity for catalyzing the decomposition of VC-mediated H_2O_2 to produce molecular oxygen (O_2) that can overcome tumor hypoxia, thus augmenting the photodynamic therapy(PDT)-induced highly toxic reactive oxygen species (ROS) production for efficient cancer cell apoptosis. The synergistic catalysis-enhanced CDT efficiency and PDT effect realized most potent tumor suppression efficacy. MnO_2@IR825-VC has achieved synergistic PTT/PDT/CDT for prostate treatment and significant inhibition of tumor growth was detected both *in vitro* and *in vivo*.

Data availability

All data generated or analyzed during this study are included in this published article. The authors are able to provide the complete raw data. The results reported in this published article can be found in the Center for Medicine Research of Shandong Provincial Third Hospital.

Conflicts of interest

There are no conflicts to declare.

Acknowledgements

This study was supported by grants from the Scientific Research and Cultivation Fund of Shandong Provincial Third Hospital (M2023005); Medical and Health Science and Technology Development Project of Shandong Province (No. 202304050369); National Natural Science Foundation of China (No. 82102040); Natural Science Foundation of Shandong Province (No. ZR2021QC056); Natural Science Foundation of Shandong Province (No. ZR2021QB174).

References

1 F. Bray, J. Ferlay, I. Soerjomataram, R. L. Siegel, L. A. Torre and A. Jemal, Global cancer statistics 2018: GLOBOCAN estimates of incidence and mortality worldwide for 36 cancers in 185 countries, *CA Cancer J. Clin.*, 2018, **68**(6), 394–424, DOI: **10.3322/caac.21492**. Erratum: F. Bray, J. Ferlay, I. Soerjomataram, R. L. Siegel, L. A. Torre and A. Jemal, Global cancer statistics 2018: GLOBOCAN estimates of incidence and mortality worldwide for 36 cancers in 185 countries, *CA Cancer J. Clin.*, 2020, **70**(4), 313, PMID: 30207593.

2 W. Chen, R. Zheng, P. D. Baade, S. Zhang, H. Zeng, F. Bray, A. Jemal, X. Q. Yu and J. He, Cancer statistics in China, 2015, *CA Cancer J. Clin.*, 2016, **66**(2), 115–132, DOI: **10.3322/caac.21338**, PMID: 26808342.

3 J. Zhang, L. Wang, X. You, T. Xian, J. Wu and J. Pang, Nanoparticle Therapy for Prostate Cancer: Overview and Perspectives, *Curr. Top. Med. Chem.*, 2019, **19**(1), 57–73, DOI: **10.2174/1568026619666190125145836**, PMID: 30686255.

4 P. Wust, B. Hildebrandt, G. Sreenivasa, B. Rau, J. Gellermann, H. Riess, R. Felix and P. M. Schlag, Hyperthermia in combined treatment of cancer, *Lancet Oncol.*, 2002, **3**(8), 487–497, DOI: **10.1016/s1470-2045(02)00818-5**, PMID: 12147435.

5 T. H. Hsu, M. E. Fidler and I. S. Gill, Radiofrequency ablation of the kidney: acute and chronic histology in porcine model, *Urology*, 2000, **56**(5), 872–875, DOI: **10.1016/s0090-4295(00)00737-8**, PMID: 11068326.

6 D. Zhi, T. Yang, J. O'Hagan, S. Zhang and R. F. Donnelly, Photothermal therapy, *J. Controlled Release*, 2020, **325**, 52–71, DOI: **10.1016/j.jconrel.2020.06.032**. Erratum: D. Zhi, T. Yang, J. O'Hagan, S. Zhang and R. F. Donnelly, Photothermal therapy, *J. Controlled Release*, 2020, PMID: 32619742.

7 X. Li, J. F. Lovell, J. Yoon and X. Chen, Clinical development and potential of photothermal and photodynamic therapies for cancer, *Nat. Rev. Clin Oncol.*, 2020, **17**(11), 657–674, DOI: **10.1038/s41571-020-0410-2**, PMID: 32699309.

8 T. W. Gong, D. A. Fairfield, L. Fullarton, D. F. Dolan, R. A. Altschuler, D. C. Kohrman and M. I. Lomax, Induction of heat shock proteins by hyperthermia and noise overstimulation in hsf1 -/- mice, *J. Assoc. Res. Otolaryngol.*, 2012, **13**(1), 29–37, DOI: **10.1007/s10162-011-0289-9**, PMID: 21932106; PMCID: PMC3254713.

9 Y. Xin, Z. Sun, J. Liu, W. Li, M. Wang, Y. Chu, Z. Sun and G. Deng, Nanomaterial-mediated low-temperature photothermal therapy via heat shock protein inhibition, *Front. Bioeng. Biotechnol.*, 2022, **10**, 1027468, DOI: **10.3389/fbioe.2022.1027468**, PMID: 36304896; PMCID: PMC9595601.

10 H. U. Simon, A. Haj-Yehia and F. Levi-Schaffer, Role of reactive oxygen species (ROS) in apoptosis induction, *Apoptosis*, 2000, **5**(5), 415–418, DOI: **10.1023/a:1009616228304**, PMID: 11256882.

11 S. Park, J. A. Park, H. Yoo, H. B. Park and Y. Lee, Proteasome inhibitor-induced cleavage of HSP90 is mediated by ROS generation and caspase 10-activation in human leukemic cells, *Redox Biol.*, 2017, **13**, 470–476, DOI: **10.1016/j.redox.2017.07.010**, PMID: 28715732; PMCID: PMC5512190.

12 B. Yang, Y. Chen and J. Shi, Nanocatalytic Medicine, *Adv. Mater.*, 2019, **31**(39), e1901778, DOI: **10.1002/adma.201901778**, PMID: 31328844.

13 T. Inoue and R. Ishihara, Photodynamic Therapy for Esophageal Cancer, *Clin. Endosc.*, 2021, **54**(4), 494–498, DOI: **10.5946/ce.2020.073**, PMID: 32422695; PMCID: PMC8357593.

14 T. Yano and K. K. Wang, Photodynamic Therapy for Gastrointestinal Cancer, *Photochem. Photobiol.*, 2020, **96**(3), 517–523, DOI: **10.1111/php.13206**, PMID: 31886891.

15 S. M. Banerjee, S. El-Sheikh, A. Malhotra, C. A. Mosse, S. Parker, N. R. Williams, A. J. MacRobert, R. Hamoudi, S. G. Bown and M. R. Keshtgar, Photodynamic Therapy in Primary Breast Cancer, *J. Clin. Med.*, 2020, **9**(2), 483, DOI: **10.3390/jcm9020483**, PMID: 32050675; PMCID: PMC7074474.

16 C. Jia, Y. Guo and F. G. Wu, Chemodynamic Therapy via Fenton and Fenton-Like Nanomaterials: Strategies and Recent Advances, *Small*, 2022, **18**(6), e2103868, DOI: **10.1002/smll.202103868**, PMID: 34729913.

17 Y. Hu, T. Lv, Y. Ma, J. Xu, Y. Zhang, Y. Hou, Z. Huang and Y. Ding, Nanoscale Coordination Polymers for Synergistic NO and Chemodynamic Therapy of Liver Cancer, *Nano Lett.*, 2019, **19**(4), 2731–2738, DOI: **10.1021/acs.nanolett.9b01093**. Erratum: Y. Hu, T. Lv, Y. Ma, J. Xu, Y. Zhang, Y. Hou, Z. Huang and Y. Ding, Nanoscale Coordination Polymers for Synergistic NO and Chemodynamic Therapy of Liver Cancer, *Nano Lett.*, 2019, **19**(11), 8342, PMID: 30919635.

18 N. M. Anderson and M. C. Simon, The tumor microenvironment, *Curr. Biol.*, 2020, **30**(16), R921–R925, DOI: **10.1016/j.cub.2020.06.081**, PMID: 32810447; PMCID: PMC8194051.

19 D. C. Singleton, A. Macann and W. R. Wilson, Therapeutic targeting of the hypoxic tumour microenvironment, *Nat. Rev. Clin Oncol.*, 2021, **18**(12), 751–772, DOI: **10.1038/s41571-021-00539-4**, PMID: 34326502.

20 X. Li, S. Lee and J. Yoon, Supramolecular photosensitizers rejuvenate photodynamic therapy, *Chem. Soc. Rev.*, 2018, **47**(4), 1174–1188, DOI: **10.1039/c7cs00594f**, PMID: 29334090.

21 B. Ma, Y. Zhao, X. Liu, M. Huo, J. Wang, J. Ma, Y. Zhang and C. Qin, Key Modulation of ROS and HSP for Effective Therapy Against Hypoxic Tumor with Multifunctional Nanosystem, *Int. J. Nanomed.*, 2023, **18**, 6829–6846, DOI: **10.2147/IJN.S432928**, PMID: 38026539; PMCID: PMC10664717.

22 A. M. Rkein and D. M. Ozog, Photodynamic therapy, *Dermatol. Clin.*, 2014, **32**(3), 415–425, DOI: **10.1016/j.det.2014.03.009**, PMID: 24891062.

23 B. Yuan, H. Wang, J. F. Xu and X. Zhang, Activatable Photosensitizer for Smart Photodynamic Therapy Triggered by Reactive Oxygen Species in Tumor Cells, *ACS Appl. Mater. Interfaces*, 2020, **12**(24), 26982–26990, DOI: **10.1021/acsami.0c07471** PMID: 32432853.

24 Z. J. Zhang, K. P. Wang, J. G. Mo, L. Xiong and Y. Wen, Photodynamic therapy regulates fate of cancer stem cells through reactive oxygen species, *World J. Stem Cells*, 2020, **12**(7), 562–584, DOI: **10.4252/wjsc.v12.i7.562**, PMID: 32843914; PMCID: PMC7415247.

25 C. M. Doskey, V. Buranasudja, B. A. Wagner, J. G. Wilkes, J. Du, J. J. Cullen and G. R. Buettner, Tumor cells have decreased ability to metabolize H_2O_2: Implications for pharmacological ascorbate in cancer therapy, *Redox Biol.*, 2016, **10**, 274–284, DOI: **10.1016/j.redox.2016.10.010**, PMID: 27833040; PMCID: PMC5106370.

26 J. Kim, S. D. Lee, B. Chang, D. H. Jin, S. I. Jung, M. Y. Park, Y. Han, Y. Yang, K. Il Kim, J. S. Lim, Y. S. Kang and M. S. Lee, Enhanced antitumor activity of vitamin C via p53 in cancer cells, *Free Radicals Biol. Med.*, 2012, **53**(8), 1607–1615, DOI: **10.1016/j.freeradbiomed.2012.07.079**, PMID: 22892142.

27 D. Erudaitius, A. Huang, S. Kazmi, G. R. Buettner and V. G. Rodgers, Peroxiporin Expression Is an Important Factor for Cancer Cell Susceptibility to Therapeutic H_2O_2: Implications for Pharmacological Ascorbate Therapy, *PLoS One*, 2017, **12**(1), e0170442, DOI: **10.1371/journal.pone.0170442**, PMID: 28107421; PMCID: PMC5249139.

28 W. Fan, W. Bu, B. Shen, Q. He, Z. Cui, Y. Liu, X. Zheng, K. Zhao and J. Shi, Intelligent MnO_2 Nanosheets Anchored with Upconversion Nanoprobes for Concurrent pH-/H_2O_2-Responsive UCL Imaging and Oxygen-Elevated Synergetic Therapy, *Adv. Mater.*, 2015, **27**(28), 4155–4161, DOI: **10.1002/adma.201405141**, PMID: 26058562.

29 F. Pi, X. Deng, Q. Xue, L. Zheng, H. Liu, F. Yang and T. Chen, Alleviating the hypoxic tumor microenvironment with MnO_2-coated CeO_2 nanoplatform for magnetic resonance imaging guided radiotherapy, *J. Nanobiotechnol.*, 2023, **21**(1), 90, DOI: **10.1186/s12951-023-01850-1**, PMID: 36922836; PMCID: PMC10018832.

30 S. S. Wan, Q. Cheng, X. Zeng and X. Z. Zhang, A Mn(III)-Sealed Metal-Organic Framework Nanosystem for Redox-Unlocked Tumor Theranostics, *ACS Nano*, 2019, **13**(6), 6561–6571, DOI: **10.1021/acsnano.9b00300**, PMID: 31136707.

31 Z. Chen, B. Peng, J. Q. Xu, X. C. Xiang, D. F. Ren, T. Q. Yang, S. Y. Ma, K. Zhang and Q. M. Chen, A non-surfactant self-templating strategy for mesoporous silica nanospheres: beyond the Stöber method, *Nanoscale*, 2020, **12**(6), 3657–3662, DOI: **10.1039/c9nr10939k**, PMID: 32016276.